ADVANCED FUNCTIONAL MATERIALS

Supporting Information

Multisensory Ferroelectric Semiconductor Synapse for Neuromorphic Computing

Jinhua Zeng, Guangdi Feng, Guangjian Wu*, Jianquan Liu, Qianru Zhao, Huiting Wang, Shuaiqin Wu, Xudong Wang, Yan Chen, Suting Han, Bobo Tian*, Chungang Duan, Tie Lin, Jun Ge, Hong Shen, Xiangjian Meng, Junhao Chu and Jianlu Wang*

Supporting Information

Multisensory Ferroelectric Semiconductor Synapse for Neuromorphic Computing

Jinhua Zeng, Guangdi Feng, Guangjian Wu,* Jianquan Liu, Qianru Zhao, Huiting Wang, Shuaiqin Wu, Xudong Wang, Yan Chen, Suting Han, Bobo Tian,* Chungang Duan, Tie Lin, Jun Ge, Hong Shen, Xiangjian Meng, Junhao Chu, and Jianlu Wang*
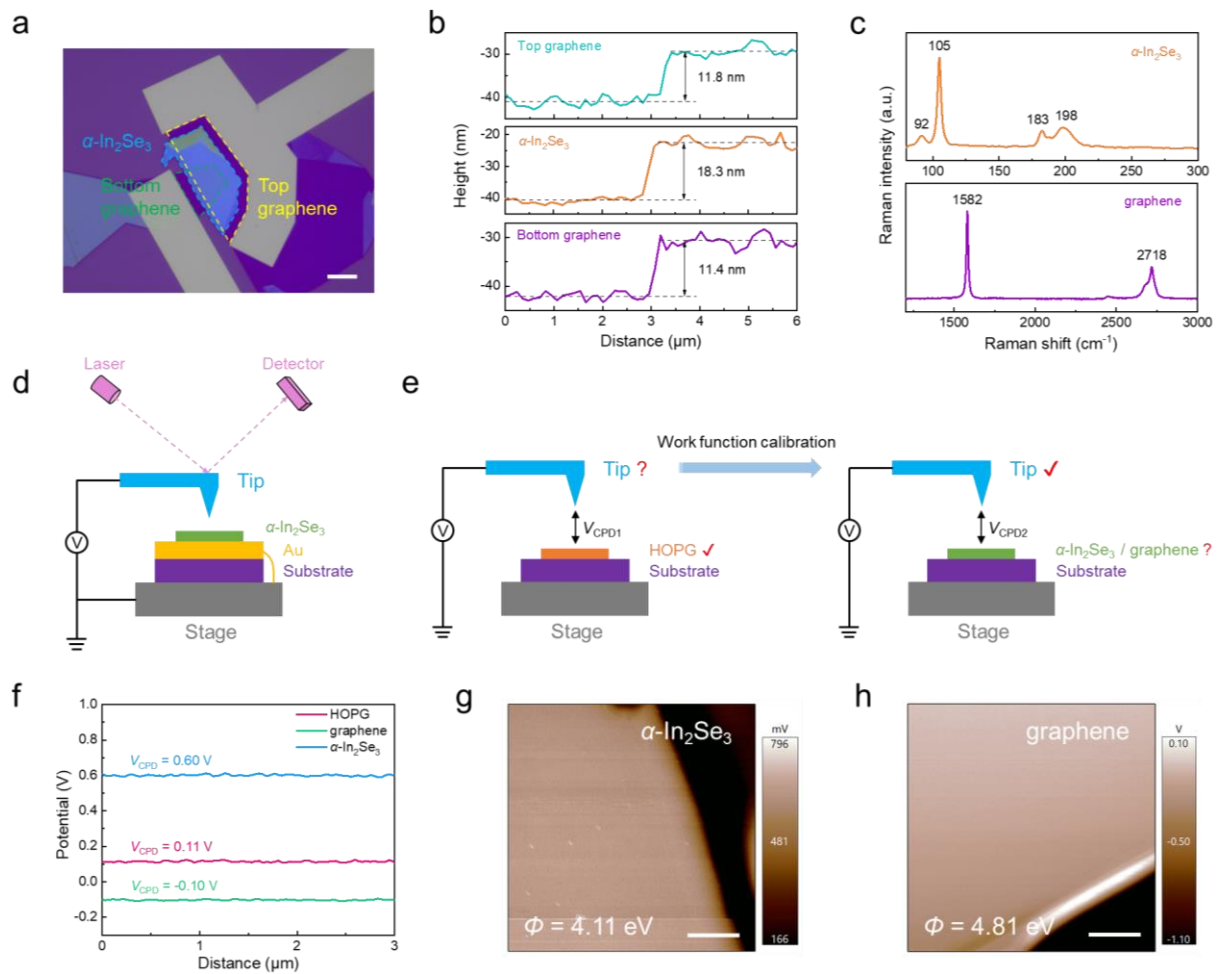
Figure S1. Device structure and material characterization. a) Microscopic optical image of two-terminal graphene/α-In$_2$Se$_3$/graphene device. Scale bar: 10 μm. b) AFM height profile for the top graphene, α-In$_2$Se$_3$ and bottom graphene, respectively. c) Raman spectrum for α-In$_2$Se$_3$ and graphene flakes on Si/SiO$_2$ substrate. d) Schematic diagram of the PFM test principle used for characterizing the ferroelectricity of materials. e) Calibration process of KPFM probes and schematic illustration of the principle for determining material work function information using KPFM technology. f) V_{CPD} data for HOPG, graphene, and α-In$_2$Se$_3$ obtained through KPFM mapping with the same tip. The work function for standard sample HOPG is typically about 4.6 eV.[1,2] g-h) KPFM mapping images of α-In$_2$Se$_3$ and graphene. Scale bar: 2 μm. The derived work functions from KPFM results are 4.11 eV and 4.81 eV, respectively.
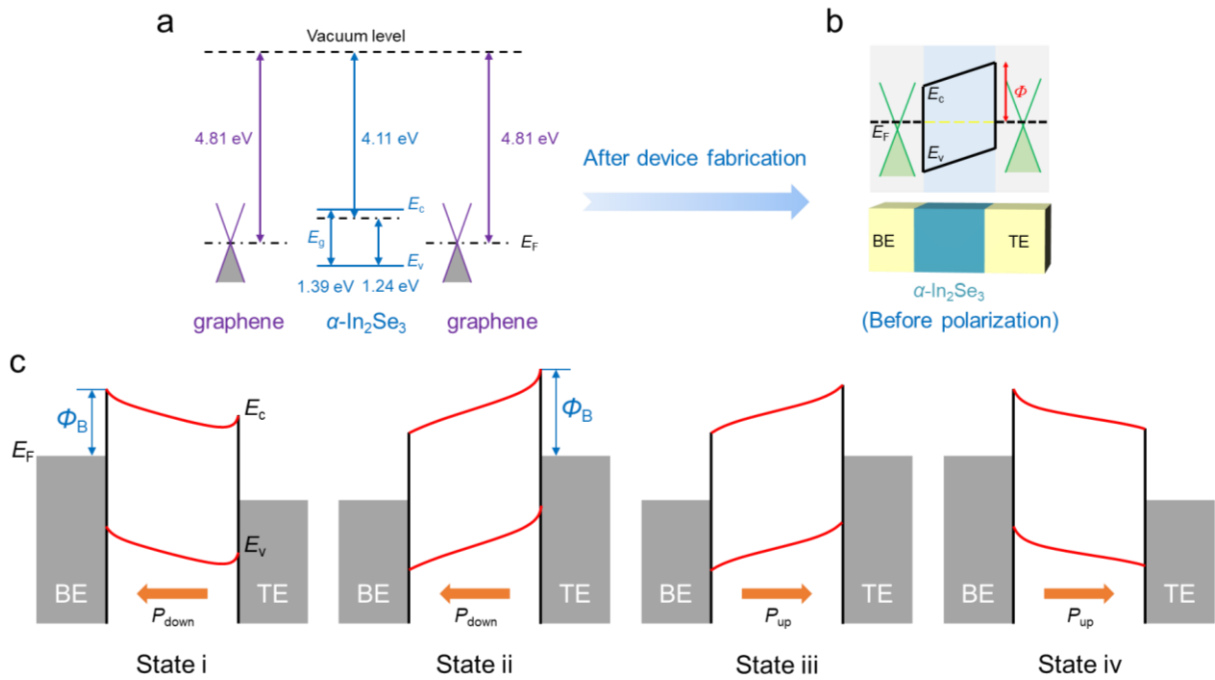

Figure S2. Schematic of energy band structure of the graphene/α-In$_2$Se$_3$/graphene device. a) Schematic of energy band alignment for α-In$_2$Se$_3$ and graphene before contact, with work function and band gap indicated.[3] b) After the fabrication of the graphene/α-In$_2$Se$_3$/graphene device, a schematic diagram of the band structure in the unpolarized states. c) Energy band diagrams illustrating the modulation of Schottky barrier height by ferroelectric polarization. States i-iv align with those described in Figure 2b in the article.
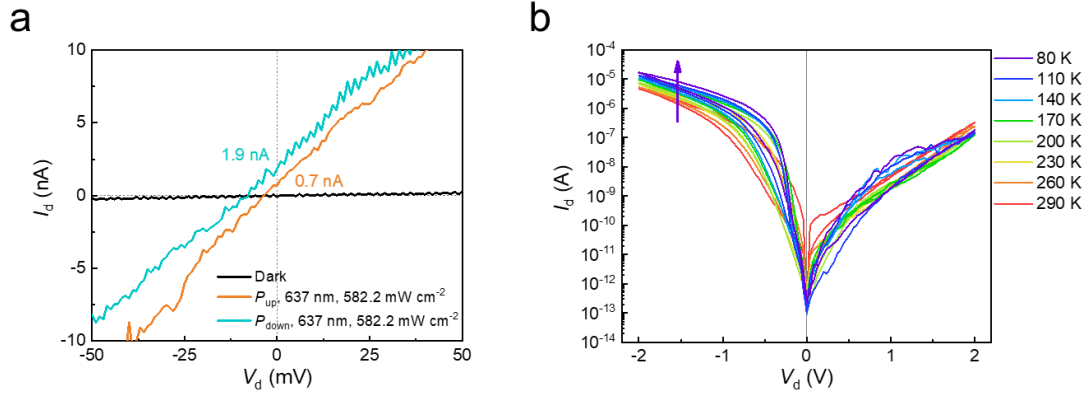
Figure S3. I_d-V_d curves under illumination and at various temperatures. a) I_d-V_d curves under illumination at small bias for different polarization states. b) Temperature-dependent I_d-V_d characteristics of α-In$_2$Se$_3$ device in darkness, ranging from 290 K to 80 K.
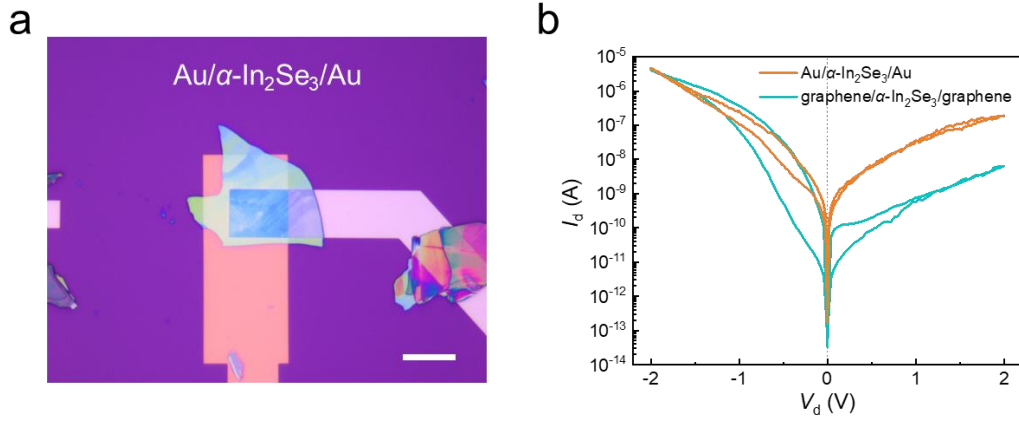

Figure S4. The crossbar structure device with direct contact between gold electrodes and α-In$_2$Se$_3$, and its I_d-V_d curve. a) The device structure of Au/α-In$_2$Se$_3$/Au prepared using transferred gold electrode technology as a control group. Scale bar: 15 μm. b) The I_d-V_d curve corresponding to the Au/α-In$_2$Se$_3$/Au device.
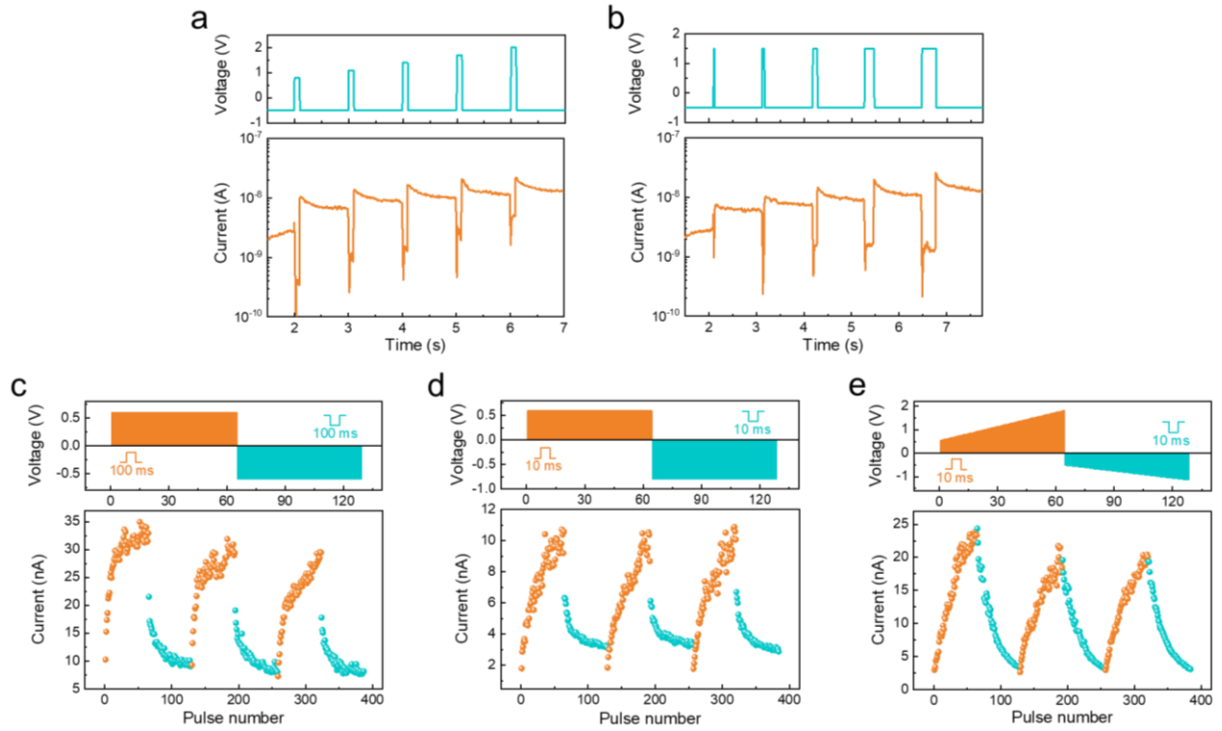
Figure S5. Electronic synaptic properties modulated by varying electrical pulse amplitude and width. a) STP response to electrical pulses of differing amplitudes (0.8, 1.1, 1.4, 1.7, and 2 V, 100 ms) with -0.5 V bias for state reading. b) STP response to electrical pulses of varied widths (20, 50, 100, 200 and 300 ms, 1.5 V) with -0.5 V bias for state reading. c) Three cycles of stable synaptic response to alternating 64 positive pulses (0.6 V, 100 ms) and 64 negative pulses (-0.6 V, 100 ms), mimicking LTP and LTD synaptic behaviors, using a -0.5 V bias for state reading. d) Three cycles of stable synaptic response to alternating 64 positive pulses (0.6 V, 10 ms) and 64 negative pulses (-0.8 V, 10 ms), emulating LTP and LTD synaptic behaviors, utilizing a -0.5 V bias for state reading. e) Three cycles of stable synaptic response to alternating 64 positive pulses (amplitude ranging from 0.56 to 1.82 V, 10 ms) and 64 negative pulses (amplitude ranging from -0.52 to -1.15 V, 10 ms), illustrating more linear LTP and LTD synaptic behaviors, with a -0.5 V bias for state reading.
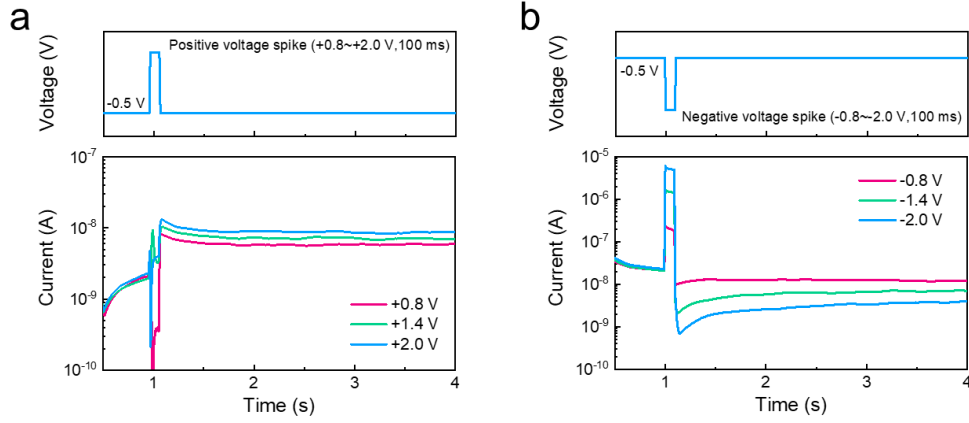
Figure S6. Time-resolved EPSC/IPSC curves for varying amplitudes. a) EPSC response from an electronic synapse under pulses of 0.8, 1.4, and 2.0 V amplitude (100 ms width), with -0.5 V bias for state reading. The current rises, stabilizes, and becomes clearly distinguishable, suggesting non-volatile intermediate states. b) IPSC response from an electronic synapse under pulses of -0.8, -1.4, and -2.0 V amplitude (100 ms width), with -0.5 V bias for state reading. The current decreases, stabilizes, and becomes clearly distinguishable, pointing to non-volatile intermediate states.
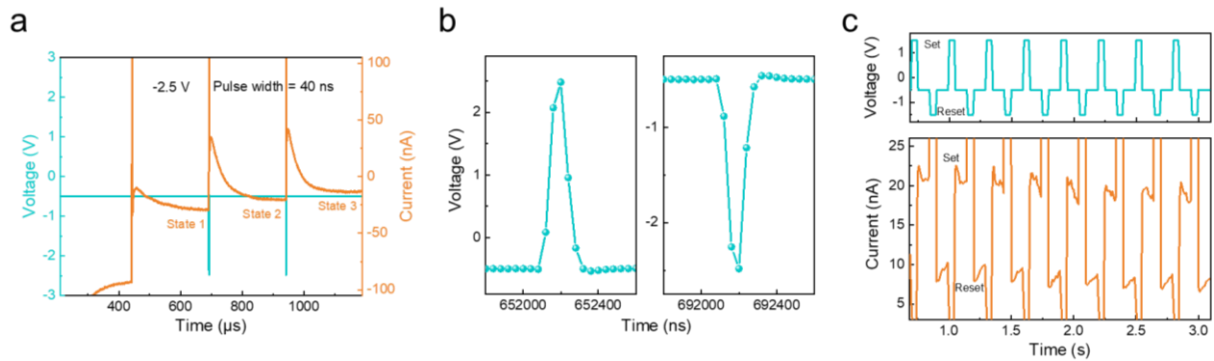

Figure S7. Ultrafast write/erase programmability and loop operations. a) Response of the device to multiple 40 ns (-2.5 V) erase spikes, illustrating ultrafast programmability. b) Schematic of a 40 ns ultrafast write/erase spike waveform. c) Dynamic response of the α-In$_2$Se$_3$ device to V_d pulses of ±1.5 V, with a -0.5 V bias for state reading.
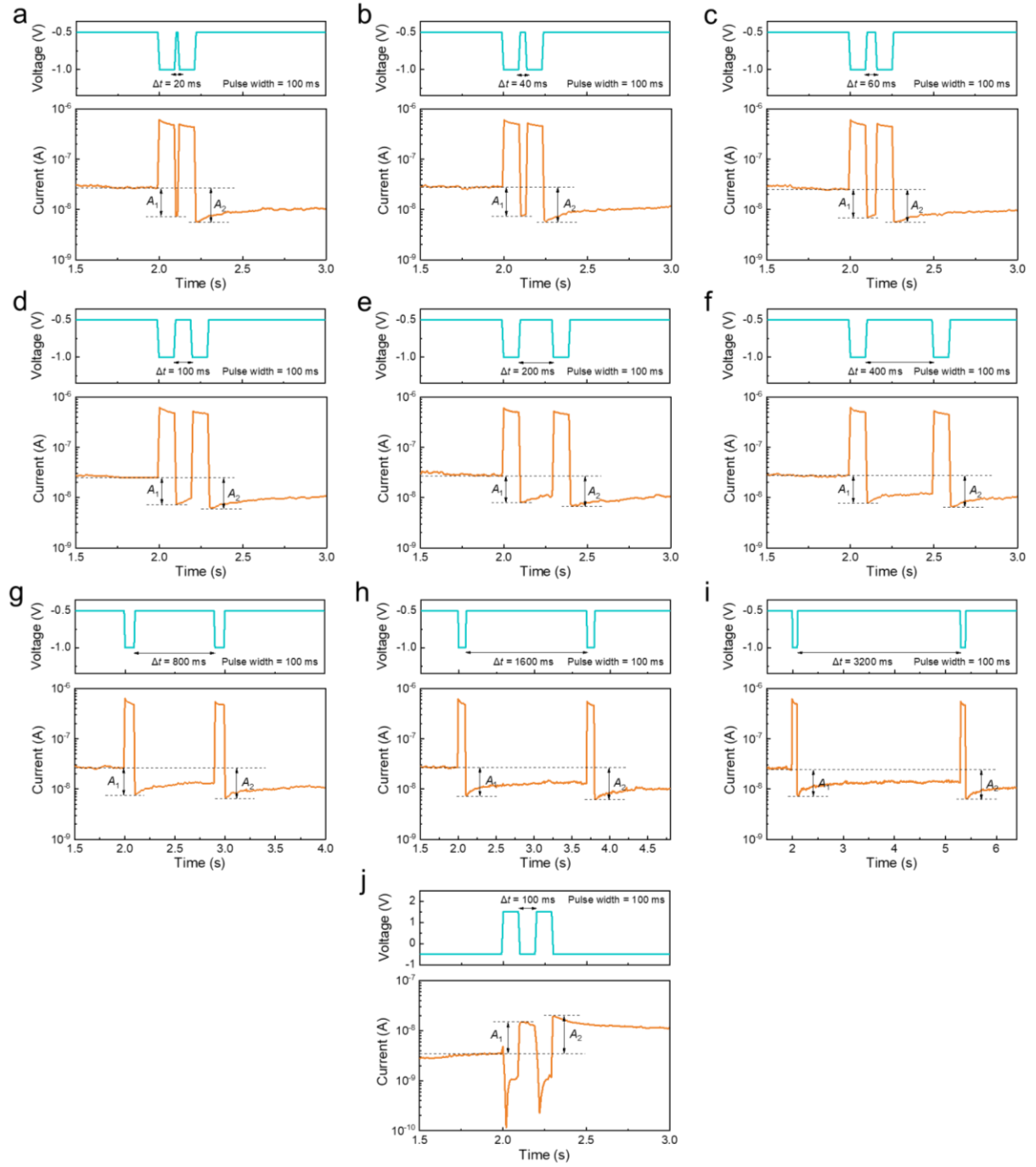
Figure S8. PPF/PPD characteristics of electronic synaptic device. a-i) PPD effect demonstrated by applying a pair of pulses (-1 V, 100 ms) with varying intervals ranging from 20 to 3200 ms, and a -0.5 V bias for state reading. j) PPF effect shown by applying a pair of pulses (+1 V, 100 ms) with a 100 ms interval, and a -0.5 V bias to read the device state.
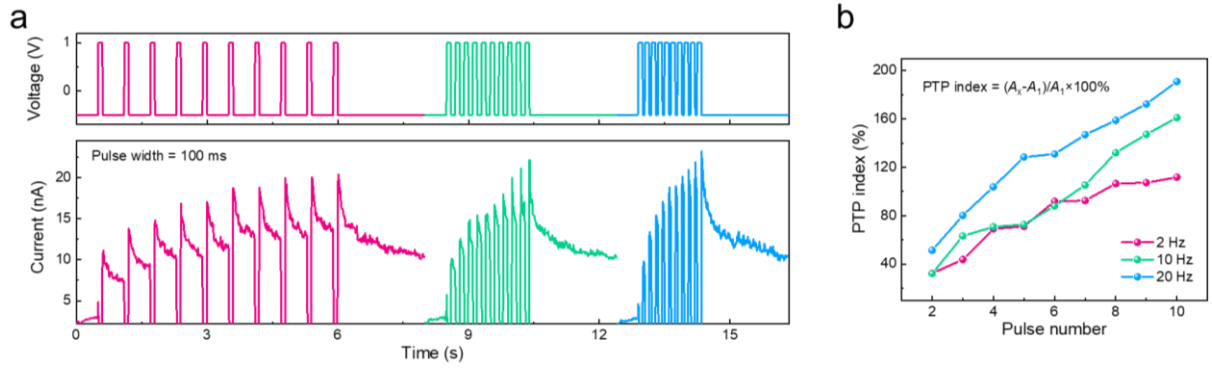
Figure S9. PTP characteristics at varying frequencies. a) EPSC response to a train of pulses (1 V, 100 ms) at frequencies of 2, 10, and 20 Hz, with -0.5 V bias for state reading. b) Data derived from a) with the PTP index calculated as $(A_x-A_1)/A_1\times100\%$,[4,5] indicating a more pronounced accumulation effect at higher stimulus frequencies.
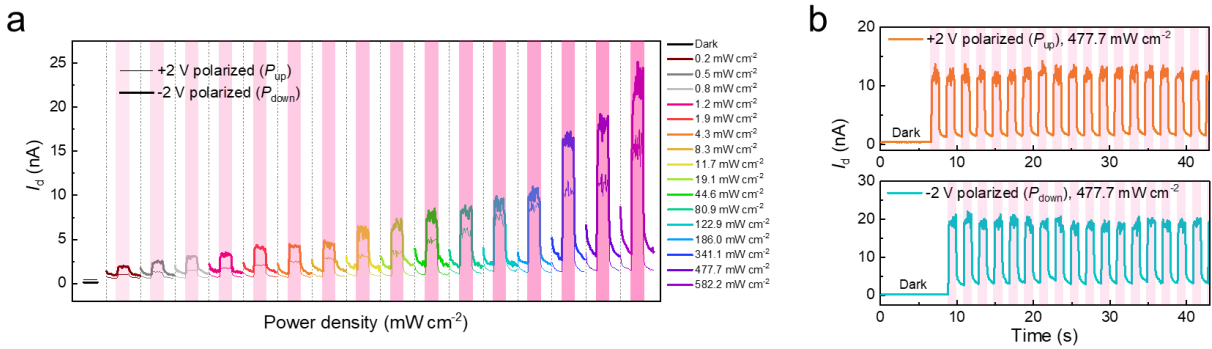
**Figure S10.** The regulation of the optoelectronic properties of the device by either upward or downward polarization states. a) Time-resolved photocurrent for P_{up}/P_{down} state under 637 nm incident light, and power density ranges from 0.2 to 582.2 mW cm^{-2} with 0.1 V bias for state reading. b) Comparison of continuous chopper photoresponse tests for different polarization directions at room temperature.
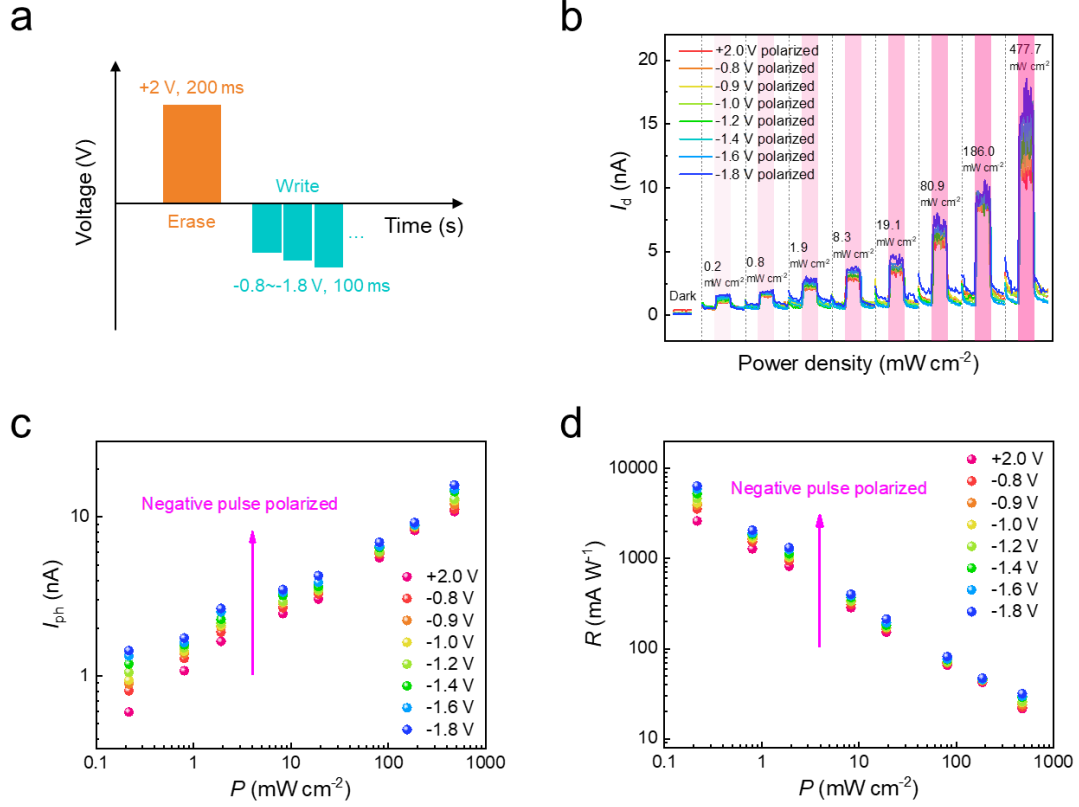
Figure S11. Regulation of photoelectric properties by various polarization states. a) Diagram illustrating the applied voltage waveform. To achieve different intermediate polarization states, the write pulse amplitude varies from -0.8 to -1.8 V. b) Time-resolved photocurrent across different intermediate polarization states under 637 nm incident light at varying power levels, with 0.1 V bias for state reading. c-d) Power dependency graphs for photocurrent and photoresponsivity under a 637 nm incident light across different intermediate polarization states.
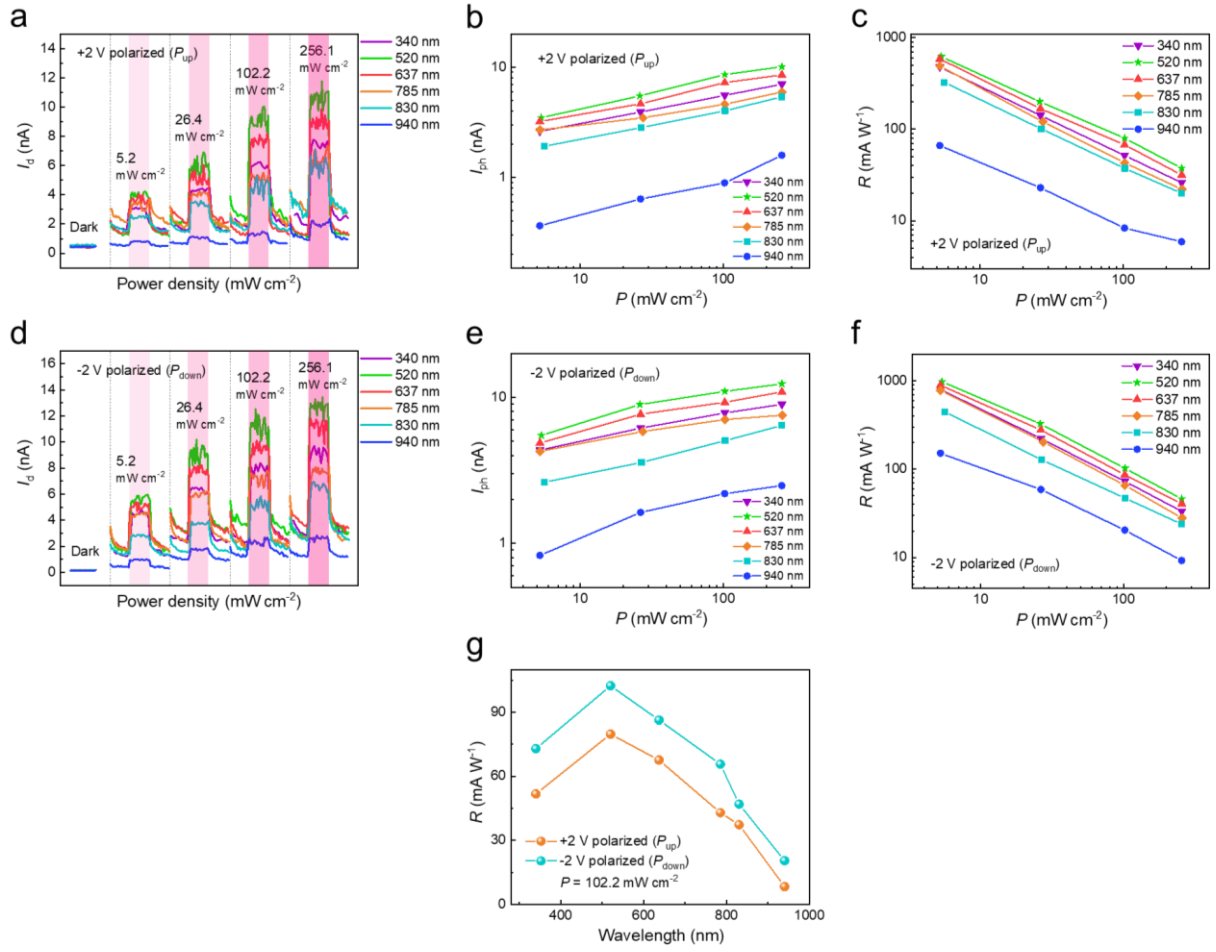
Figure S12. Photoelectric characteristics across varying incident light wavelengths. a) Time-resolved photocurrent in the P_{up} state for incident light wavelengths of 340, 520, 637, 785, 830, and 940 nm at variable power levels, measured with a 0.1 V bias. b-c) Power-dependent variations in photocurrent and photoresponsivity in the P_{up} state for the given wavelengths. d) Time-resolved photocurrent in the P_{down} state for incident light wavelengths of 340, 520, 637, 785, 830, and 940 nm at varied power levels, taken with a 0.1 V bias. e-f) Power-dependent variations in photocurrent and photoresponsivity in the P_{down} state for the specified wavelengths. g) Wavelength-dependent photoresponsivity under different polarization directions.
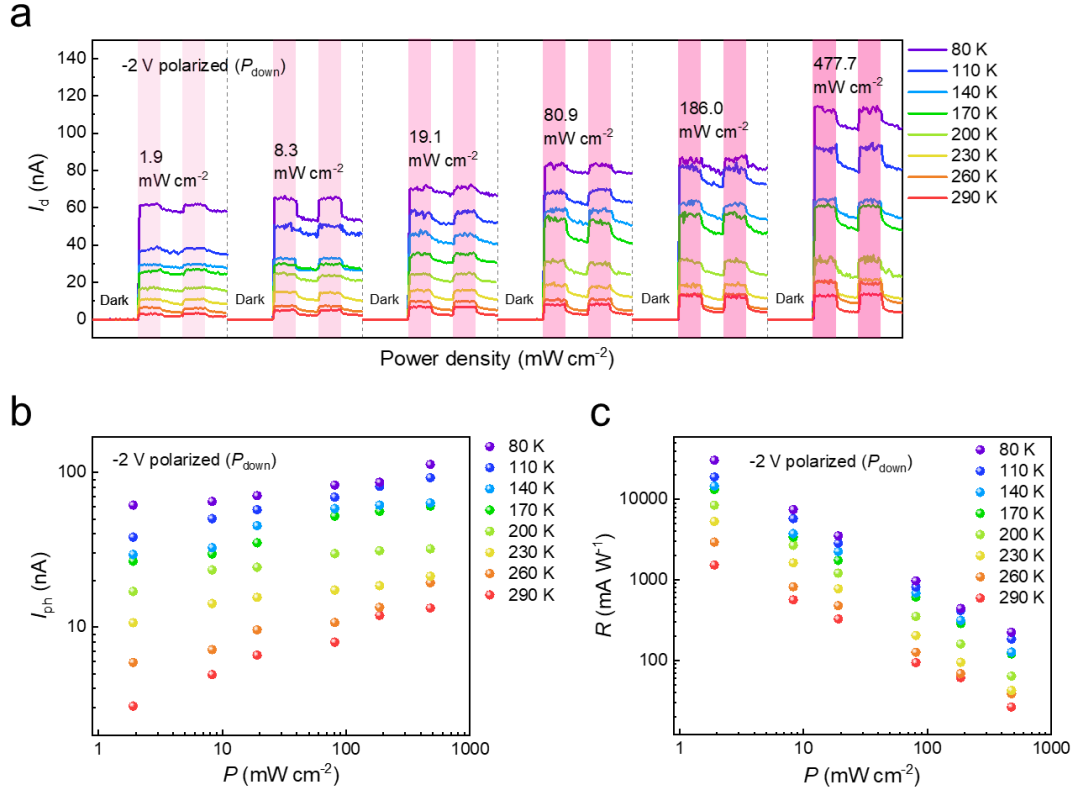
Figure S13. Photoelectric characteristics across varied temperatures. a) Time-resolved photocurrent in the P_{down} state at temperatures of 290, 260, 230, 200, 170, 140, 110, and 80 K, measured under different power levels with a 0.1 V bias. b-c) Power-dependent photocurrent and photoresponsivity in the P_{down} state at these temperatures.
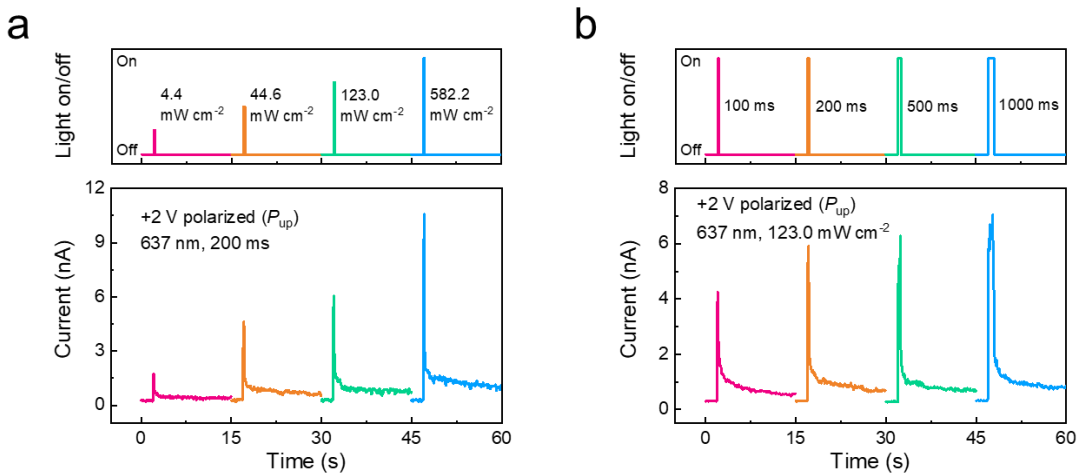
Figure S14. PSC profiles corresponding to optical pulses with varied amplitudes and widths. a) PSC response to optical pulses of varying amplitudes (4.4, 44.6, 123.0, and 582.2 mW cm^{-2}) with a duration of 200 ms, applied to the device in the P_{up} state under a 0.1 V bias for state

reading. b) PSC response to optical pulses with different durations (100, 200, 500, and 1000 ms) at 123.0 mW cm^{-2}, applied to the device in the P_{up} state under a 0.1 V bias for reading the device state.
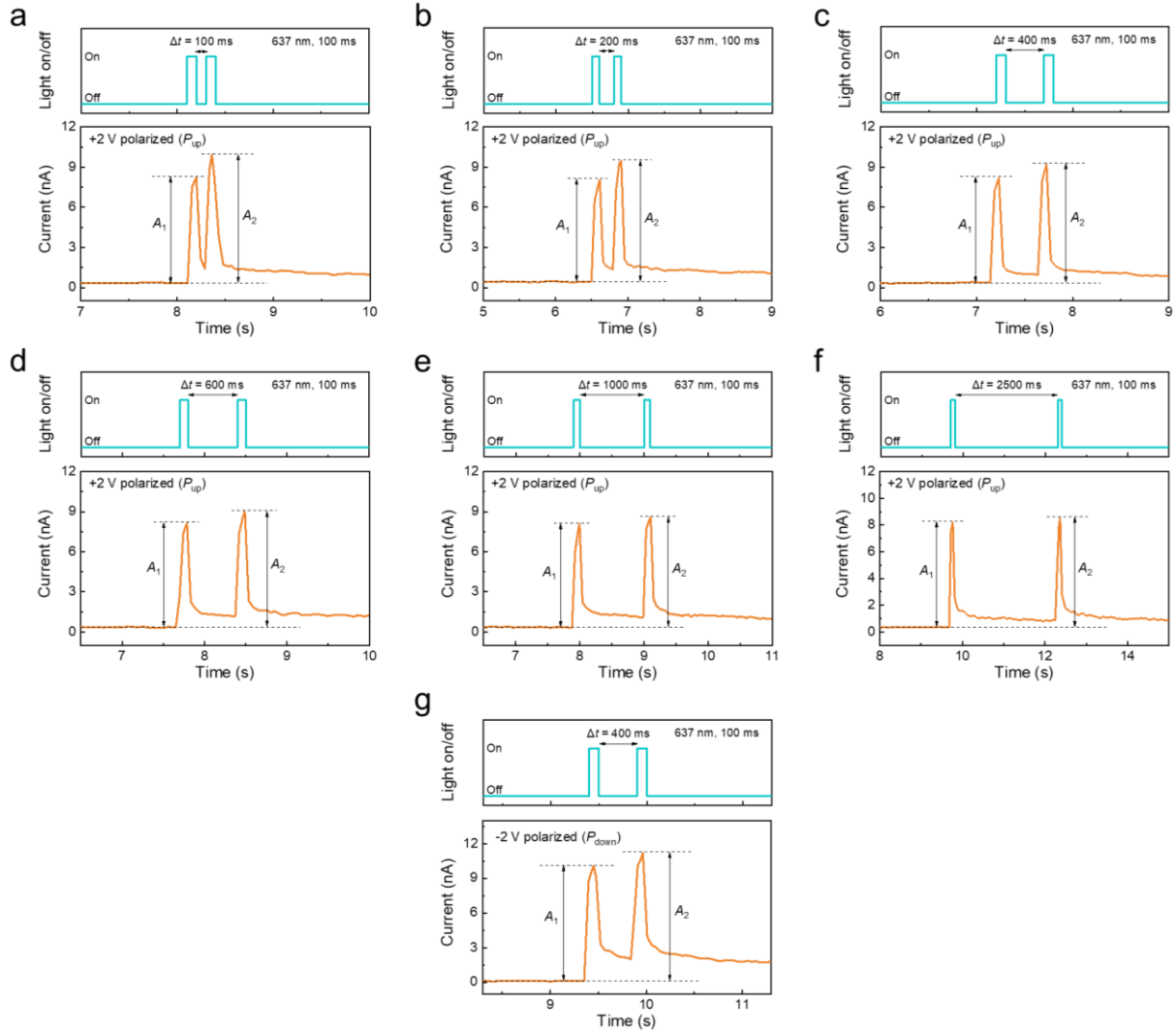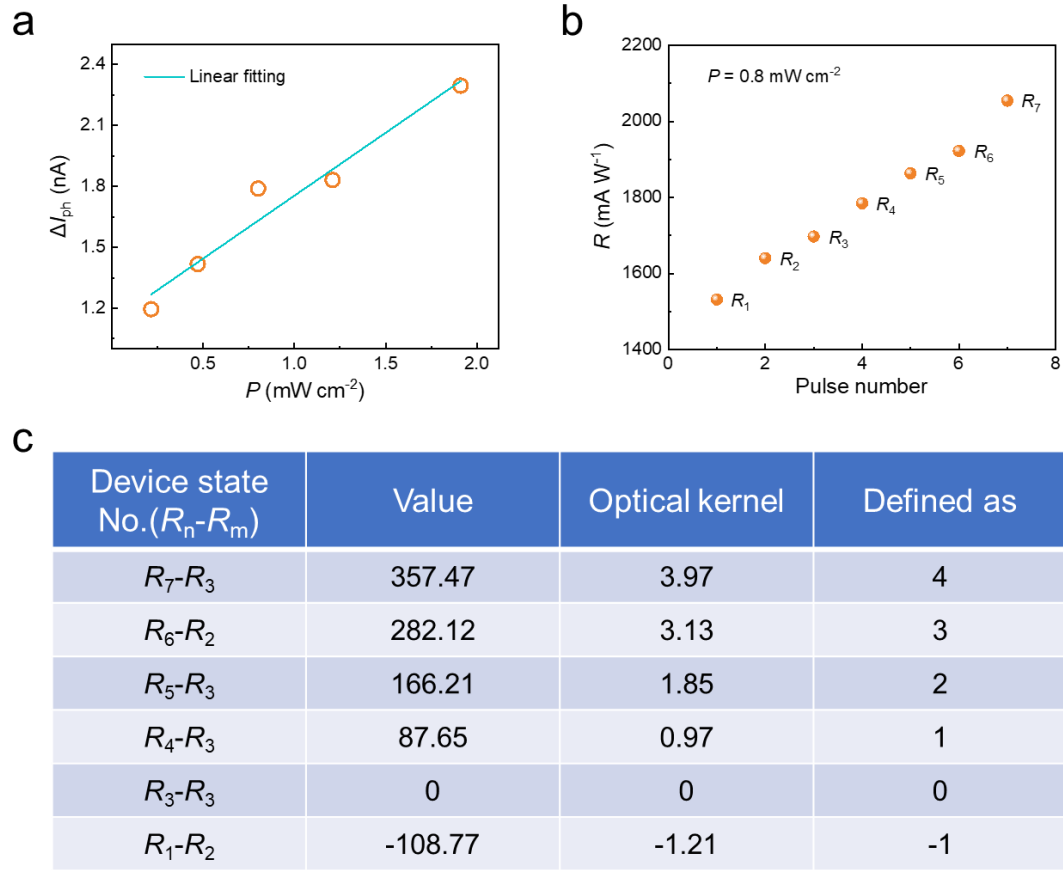

Figure S15. PPF characteristics of optoelectronic synaptic device. a-f) PPF effect observed when applying a pair of optical pulses (637 nm, 100 ms) with varying intervals ranging from 100 ms to 2500 ms at the P_{up} state, reading at 0.1 V bias. g) PPF effect demonstrated by a pair of optical pulses (637 nm, 100 ms) with a 400 ms interval applied at the P_{down} state, reading at 0.1 V bias.

Device state No.(R_n-R_m)	Value	Optical kernel	Defined as
R_7-R_3	357.47	3.97	4
R_6-R_2	282.12	3.13	3
R_5-R_3	166.21	1.85	2
R_4-R_3	87.65	0.97	1
R_3-R_3	0	0	0
R_1-R_2	-108.77	-1.21	-1

Figure S16. Definition of the device's photoresponsivity states and convolution kernel parameters. a) Linear fitting of photoresponsivity difference (ΔI_{ph}) in low power range. b) Definition of the device's photoresponsivity states. c) Utilize the difference of the device photoresponsivity weights to sequentially define the convolutional kernel parameters from 4 to -1.

a

Device state No.(R_n-R_m)			Optical kernel			Ideal kernel		
R_3-R_3	R_1-R_2	R_3-R_3	0	-1.21	0	0	-1	0
R_1-R_2	R_7-R_3	R_1-R_2	-1.21	3.97	-1.21	-1	4	-1
R_3-R_3	R_1-R_2	R_3-R_3	0	-1.21	0	0	-1	0

b

R_3	R_1	R_3
R_1	R_7	R_1
R_3	R_1	R_3

−

R_3	R_2	R_3
R_2	R_3	R_2
R_3	R_2	R_3

=

0	-1	0
-1	4	-1
0	-1	0

Figure S17. Optical convolution kernel extraction process. a) The comparison between optical convolution kernel and ideal convolution kernel. b) The matrix parameters of the convolution kernel used can be equivalently considered as the difference derived from two distinct photoresponsivity matrices.
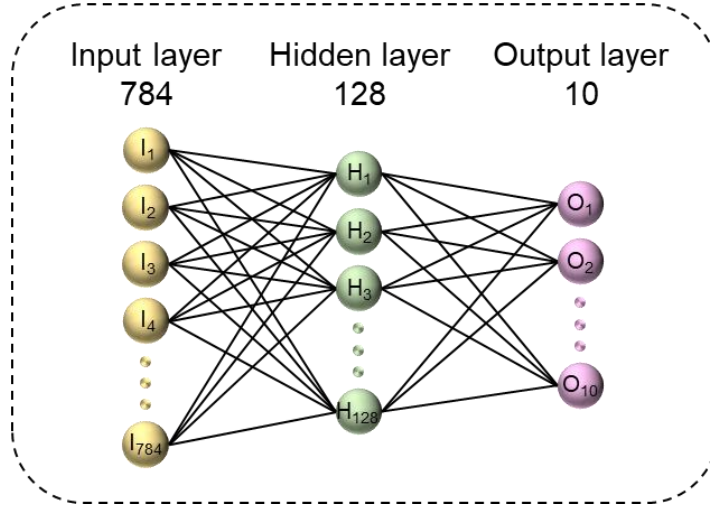
Figure S18. A fully connected ANN, constructed using the α-In$_2$Se$_3$ synaptic properties, comprises an input layer, a hidden layer, and an output layer, and is utilized for advanced image recognition tasks.

a Epoch 0: first layer   Epoch 25: first layer

b Epoch 0: second layer   Epoch 25: second layer
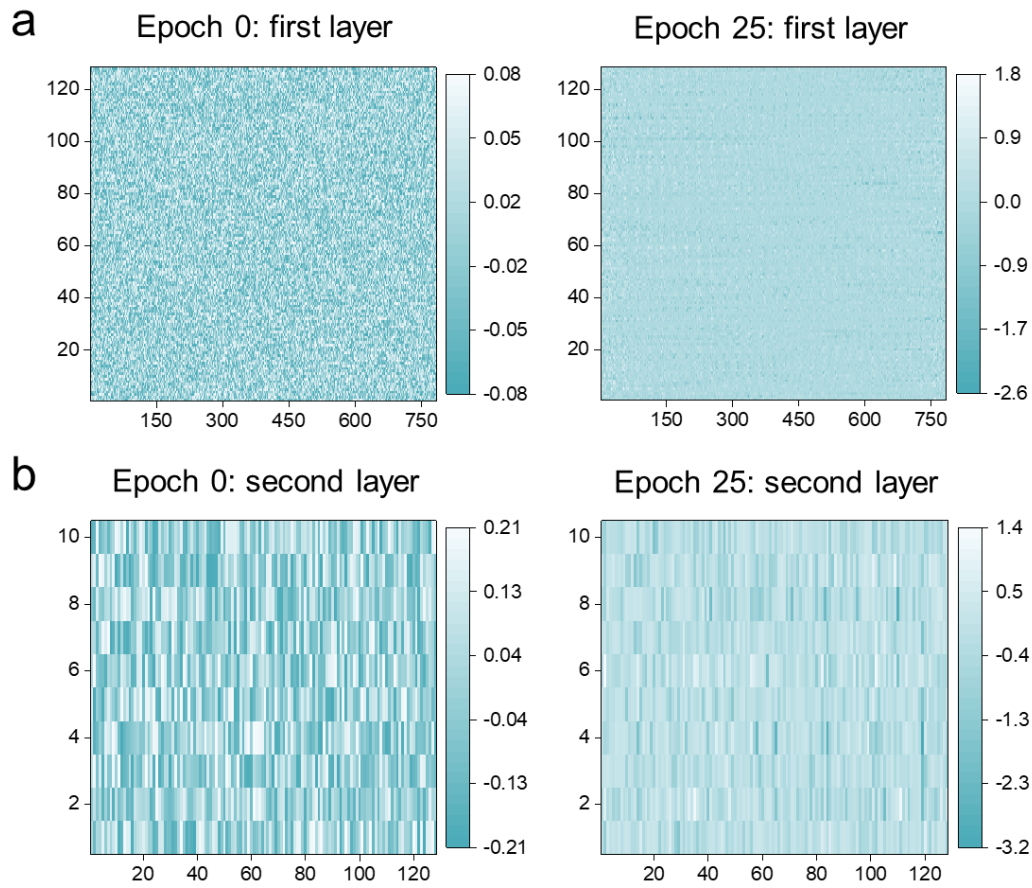
Figure S19. Initial weights and intermediate weights after 25 training epochs. a) Distribution of the first layer weights: x-axis shows 784 (28×28) reservoir states, and y-axis denotes 128 output classes. b) Distribution of the second layer weights: x-axis displays 128 reservoir states, while y-axis indicates 10 output classes.

Note S1. The CNN code of image recognition process.

```
import os
import cv2
import numpy as np
from PIL import Image
kernel = np.array([[0, -1, 0],
              [-1, 4, -1],
              [0, -1, 0]])
```

```
Input_folder = "…/cross-sim-main/Image"

output_folder = "…/cross-sim-main/output_images_folder"

if not os.path.exists(output_folder):

    os.makedirs(output_folder)

for filename in os.listdir(input_folder):

    if filename.endswith(".jpg") or filename.endswith(".png"):

        input_path = os.path.join(input_folder, filename)

        output_path = os.path.join(output_folder, filename)

        image = cv2.imread(input_path)

        convolved_image = cv2.filter2D(image, -1, kernel)

        cv2.imwrite(output_path, convolved_image)

print
```

References

[1]   S.-H. Lee, S. W. Lee, T. Oh, S. H. Petrosko, C. A. Mirkin, J.-W. Jang, *Nano Lett.* **2018**, *18*, 109.

[2]   S. Aftab, Samiya, Rabia, S. Yousuf, M. U. Khan, R. Khawar, A. Younus, M. Manzoor, M. W. Iqbal, M. Z. Iqbal, *Nanoscale* **2020**, *12*, 15687.

[3]   J. Wang, C. Liu, L. Zhang, J. Chen, J. Chen, F. Yu, Z. Zhao, W. Tang, X. Li, S. Zhang, G. Li, L. Wang, Y. Cheng, X. Chen, *Adv. Sci.* **2023**, *10*, 2205813.

[4]   H. Zhong, Q.-C. Sun, G. Li, J.-Y. Du, H.-Y. Huang, E.-J. Guo, M. He, C. Wang, G.-Z. Yang, C. Ge, K.-J. Jin, *Chin. Phys. B* **2020**, *29*, 040703.

[5]   S. Hao, S. Zhong, X. Ji, K. Y. Pang, N. Wang, H. Li, Y. Jiang, K. G. Lim, T. C. Chong, R. Zhao, D. K. Loke, *ACS Appl. Mater. Interfaces* **2021**, *13*, 60209.